Obrabotka metallov (tekhnologiya, oborudovanie, instrumenty) = Metal Working and Material Science. 2026 vol. 28 no. 2 pp. 72–98
ISSN: 1994-6309 (print) / 2541-819X (online)
DOI: 10.17212/1994-6309-2026-28.2-72-98

NSTU NETI

Obrabotka metallov - Metal Working and Material Science

Journal homepage: http://journals.nstu.ru/obrabotka_metallov

Cutting forces, chip morphology and wear characteristics in milling of Inconel 625 alloy produced by EBAM

Artem Babaev [a, *], ***Viktor Kozlov*** [b], ***Nikolai Savchenko*** [c], ***Artem Semenov*** [d], ***Roman Tsygankov*** [e]

National Research Tomsk State University, 36 Lenin Avenue, Tomsk, 634050, Russian Federation

[a] https://orcid.org/0000-0003-2334-1679, temkams@mail.ru; [b] https://orcid.org/0000-0001-9351-5713, kozlov-victor@bk.ru;
[c] https://orcid.org/0000-0001-8254-5853, savnick@ispms.ru; [d] https://orcid.org/0000-0002-8663-4877, artems2102@yandex.ru;
[e] https://orcid.org/0000-0002-2660-2312, tsygankovrs@gmail.com

ARTICLE INFO

Article history:
Received: 24 March 2026
Revised: 11 April 2026
Accepted: 14 April 2026
Available online: 15 June 2026

Keywords:
Inconel 625
Milling
Additive technologies
Cutting force
Chip
Wear

Funding
The work was supported by the Russian Science Foundation (project No. 23-79-10166, https://rscf.ru/en/project/23-79-10166/).

ABSTRACT

Introduction. Nickel-based alloys such as *Inconel 625* are widely used in the aerospace industry due to their high heat resistance and corrosion resistance. However, their machining is complicated by the low thermal conductivity of the material, its tendency to work hardening, and accelerated tool wear. The advent of additive technologies makes it possible to obtain blanks close to the final shape, but the machinability of such materials has not been sufficiently studied, especially taking into account the anisotropy of properties caused by synthesis conditions. In this regard, the study of cutting forces, the explanation of chip morphology, and the description of the causes of tool wear during milling of additively manufactured *Inconel 625* is an urgent task. **Methods.** The samples were obtained by electron beam additive manufacturing (*EBAM*) from *Inconel 625* wire. Milling was carried out with uncoated cemented carbide end mills. The cutting forces were recorded using a three-component dynamometer *Kistler mod. 9257BA*. The microstructure, chip morphology, and tool wear were studied by scanning electron microscopy using energy-dispersive analysis and X-ray diffraction analysis. **Results and discussion.** It has been found that in conventional milling, the cutting forces increase linearly with increasing feed rate. The cutting speed of 23.8 m/min reduces cutting forces compared to 11.9 m/min, but leads to an increase in chip length and deterioration of its removal. Machinability anisotropy is revealed: the cutting forces along the synthesis direction exceed the corresponding values when milling transversely across, which correlates with a higher yield strength in the longitudinal direction. The chip length increases with increasing feed rate and cutting speed, reaching 1.55 mm under maximum conditions, while the chips lose their coiled shape and become cracked. The dominant wear mechanism is adhesion-fatigue wear, confirmed by the presence of *WC* particles on the rake surface of the chips and the formation of $Cr_{23}C_6$ and *NiW* phases on the cutting edges. Oxidative wear does not play a significant role. X-ray diffraction analysis showed a decrease in the initial crystallographic texture in the chips and on the machined surface, as well as a broadening of the peaks, indicating severe plastic deformation. ***Conclusions.*** Rational milling parameters have been determined (cutting speed from 11.9 to 23.8 m/min, feed rate of no more than 200 mm/min, depth of cut up to 1 mm, width of cut up to 7 mm), ensuring tool operability. An increase in the feed rate to 250 mm/min leads to catastrophic failure of the cutting edges. The results obtained can be used to develop technological recommendations for the subtractive machining of parts made of additively manufactured *Inconel 625* (*EBAM*).

For citation: Babaev A.S., Kozlov V.N., Savchenko N.L., Semenov A.R., Tsygankov R.S. Cutting forces, chip morphology and wear characteristics in milling of Inconel 625 alloy produced by EBAM. *Obrabotka metallov (tekhnologiya, oborudovanie, instrumenty) = Metal Working and Material Science*, 2026, vol. 28, no. 2, pp. 72–98. DOI: 10.17212/1994-6309-2026-28.2-72-98. (In Russian).

Introduction

The main use of *Inconel 625* nickel alloy in aggressive environments is due to its unique ability to withstand a combination of destructive factors. These include corrosion, fatigue (including that caused by temperature changes), erosion, and creep, and the material retains these properties even under extreme temperature conditions [1]. Nickel-based alloys are considered difficult to machine. They tend to work

*** Corresponding author**
Babaev Artem S., Ph.D. (Engineering), Senior Researcher
National Research Tomsk State University,
36 Lenin Avenue,
634050, Tomsk, Russian Federation
Tel.: +7 952 805-09-26, **e-mail:** temkams@mail.ru

harden during plastic deformation, have low thermal conductivity, high heat resistance, and the hard abrasive particles in their microstructure accelerate the wear of cutting edges [2–4]. During cutting, the interaction between the tool and the workpiece causes severe plastic deformations of the workpiece, which are aggravated by the low thermal conductivity of the material, creating high cutting forces and temperatures. Such forces and thermal loads during cutting cause rapid tool wear and reduce the machining efficiency of the material [5, 6].

The above alloys are widely in demand due to their unique performance properties. Due to their high temperature resistance, they are used in conditions of critically high temperatures during operation, for example, in aircraft engines. However, the issues of machining to form the final dimensions, accuracy, and surface roughness are still relevant today, especially in connection with the emergence of new principles for the production of blanks (prototypes) from heat-resistant alloys. Let us consider in more detail the results of research on the machining efficiency of nickel-based alloys obtained both by traditional methods and using additive technologies.

In [7, 8], the milling of *Inconel 625* was investigated using as a coolant a mixture of biodegradable oils, namely castor oil and soybean oil in a 1:1 ratio, with a minimum amount of coolant (*MQL* technology). The authors used simulations for three different machining conditions, including dry machining, minimal coolant flow, and simultaneous spraying of a minimal coolant mixture along with liquid carbon dioxide and nitrogen. The results showed that cryogenic cooling together with a mixture of biodegradable materials provides the best results among all the conditions tested.

The study [9] focuses on optimizing cutting conditions and numerical analysis of flank wear during milling of *Inconel 625* superalloy using carbide inserts coated with *PVD AlTiN* and *CVD* $TiCN/Al_2O_3/TiN$. The milling experiments were carried out on a numerically controlled vertical machining center (hereinafter *CNC*) in accordance with the Taguchi orthogonal array matrix. Tool wear modeling using the finite element method was performed using the *Deform 3D* software. Analysis of variance was used to determine the effect of milling conditions on flank wear. The results showed that the feed rate is the most important parameter affecting wear. Linear and quadratic regression analyses were used to evaluate the experimental results. The regression analysis results showed that the estimated wear values calculated using the quadratic regression model were more effective than those from the linear regression model. Statistical analysis has shown that the *Taguchi* method can be used to optimize cutting parameters when milling *Inconel 625*.

For example, the main purpose of [10] is to empirically establish and statistically evaluate the effect of milling modes on ***Ra*** surface roughness and flank wear when milling *Inconel 625*. The results show that a higher correlation coefficient was obtained using a quadratic regression model with a value of 0.97 for both ***Ra*** and wear. The test results are in good agreement with experimental data on surface roughness ***Ra*** and tool wear.

Parts manufactured by the additive method can be made in a shape close to the final one, and usually only need to undergo finishing operations to ensure tolerances and surface roughness. Since heat-resistant superalloys are particularly difficult to machine, additive manufacturing technologies for the manufacture of blanks are of great interest. However, parts manufactured by the additive method exhibit different properties than their counterparts manufactured by the traditional method, including differences in machinability depending on the direction of synthesis. Modeling the cutting force for materials produced by the additive method should be designed to correctly select the machining strategy and cutting parameters. In [11], a mechanistic model is proposed for predicting the cutting force. Validation of the model output for uncut chip thickness and cross-sectional area was performed using *3D CAD* uncut chip thickness models. In-depth experimental testing was conducted to collect force data for modeling and evaluation purposes. The effects of feed, cutting speed, scanning strategy, and orientation of the cutting wedge relative to the workpiece are analyzed. The simulation results were compared with the collected experimental data, showing good agreement between the simulation and experimental results, which confirms the validity of the proposed mechanistic model for machining materials obtained by the additive method.

In [12], an analytical model of cutting force is described, which is also suitable for parts manufactured using additive manufacturing, and which takes into account the presence of cutting modes with a predominance of shear stresses. The procedure for refining the cutting force model was determined and applied by performing experimental work on *Inconel 625* samples manufactured by *LaserCUSING^{TM}*. The model has been successfully used to predict how the cutting force affects changes in the parameters of the machined surface (roughness, microhardness, etc.).

In the study [13], various grades of cemented carbide, cutting speed, and feed per tooth were evaluated to determine the rational conditions for face milling *Inconel 625*. The characteristics of the cutting tool life and wear mechanisms were analyzed based on the test results using a milling cutter with cemented carbide cutting inserts. The main results show that the mechanisms of tool wear during milling *Inconel 625* are similar to those observed in other nickel-based superalloys such as *718* and *713*. However, the wear rate is lower, and there is evidence of oxidative wear.

In the study [14], finishing during milling is considered as post-machining to improve the surface, mechanical, and wear-resistant properties of samples made by the *SLM* method. This study shows that surface and subsurface characteristics such as surface topography, surface roughness, microhardness, and wear resistance depend significantly on milling parameters.

In [15], the study focuses on detecting changes in surface roughness during *Inconel 625* face milling using cutting force monitoring. In addition, the influence of machining parameters on cutting forces and surface roughness is investigated. The study examines five levels for each cutting parameter, including feed, cutting speed, and depth of cut. To determine the surface quality, both time and frequency characteristics of the cutting force data collected during milling are used. *Bayesian*-optimized support vector machine and artificial neural network models are used, followed by their comparison. The support vector model achieved an accuracy of 99.61%, while the neural network model had an accuracy of 99.74%.

A significant number of scientific papers are focused on studying the features of milling of Inconel group alloys obtained using additive technologies *WAAM*, *LPBF*, and *SLM* [16–19].

In these papers, the authors draw attention to the relationship between the anisotropy of the workpiece properties and the resulting cutting forces, as well as tool wear and roughness of the machined surface. However, very few studies have provided empirical data on nickel-based alloys obtained using *EBAM* additive technology.

Direct transfer of the machinability results obtained for *Inconel 625 LPBF* or *WAAM* materials to *EBAM* materials cannot be applied for the following reasons:

– the scale of structural heterogeneity of *EBAM* (coarse grains, coarse carbides) creates specific dynamics of cutting forces that cannot be reproduced on fine-grained *LPBF* samples;

– the pronounced anisotropy of the yield strength of the *EBAM* material requires a separate study of the dependence of cutting forces on the milling direction, which is not relevant for isotropic or weakly anisotropic *WAAM* structures;

– the combined wear mechanism (adhesive from high adhesion forces + abrasive from large liquated carbides) is unique to *EBAM* and is not observed in its pure form either when machining *LPBF* materials (adhesion prevails) or *WAAM* materials (abrasive wear prevails).

In connection with the above, ***the aim of the work*** is formulated, which is to develop ideas about the machinability features of an additive nickel-based alloy obtained using *EBAM* technology by milling it and studying the resulting cutting forces, the morphology of the chips formed, and the wear of the cutting edges of tools. To achieve the aim***, the following tasks*** are formulated:

– to evaluate the anisotropy of machinability and the influence of the milling direction on cutting forces;

– to obtain the dependences of cutting forces on milling modes and to analyze the effect of cutting speed on chip morphology;

– to determine the dependence of chip morphology on milling modes and directions;

– to identify the dominant mechanism of tool wear during milling of additive material;

– to study the crystallographic texture and the degree of influence of oxidative wear;

– to determine rational milling modes and the boundaries of catastrophic wear.

Research methodology

On laboratory equipment at the Institute of Strength Physics and Materials Science SB RAS (Tomsk), a sample was produced using the additive technology of *EBAM* (*Electron Beam Additive Manufacturing*). For this purpose, a wire designated *OKAutrodNiCrMo-3* (*ESAB*, Sweden) with a diameter of 1.2 mm was used. A 5 mm thick steel sheet of grade *AISI 321* was used as a substrate during synthesis. The synthesis parameters were used according to the data of [20, 21], namely: accelerating voltage of 30 kV; electron beam current of 60 mA. The electron beam traveled along a circular sweep with a diameter of 6 mm at a table feed rate of 300 mm/min (Fig. 1).

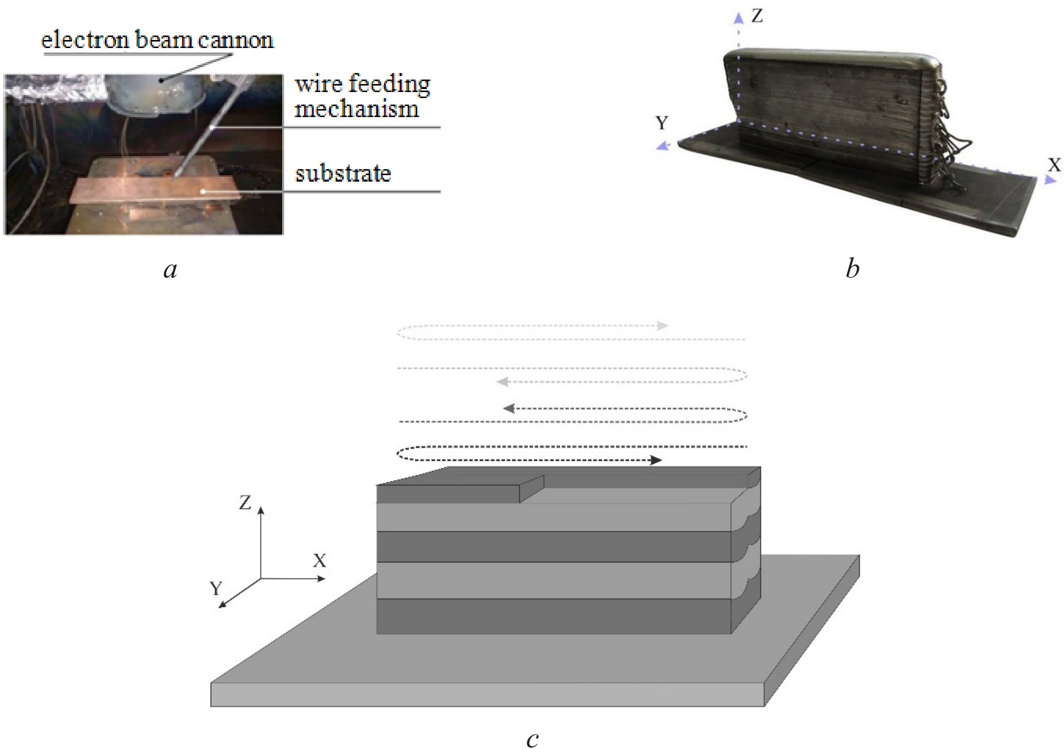

Fig. 1. Work area of the laboratory setup (*a*), appearance (*b*) of the *Inconel 625* sample, and scanning scheme (*c*)

Thus, a prototype billet was obtained, from which the crust was removed by electro-erosion wire cutting, and 50 × 50 × 16 mm samples were obtained for mechanical and metallographic testing, as well as for milling (Fig. 2). To verify the repeatability of the microstructure and physico-mechanical properties affecting the cutting process, a series of samples was prepared under similar conditions. The test results were comparable (the difference in readings was 10–15%).

The forces were recorded using a three-component dynamometer model *9257BA* from *Kistler* (Switzerland). The latter was mounted on a milling machine table, and an additive billet was fixed on top in a special device. Data collection took place at a frequency of 5–10 kHz during 5–10 seconds – the time required for all teeth of the milling cutter to enter the workpiece. For each cutting mode, 4–5 repetitions were performed when measuring cutting forces, and the average of the highest values was calculated. The difference in readings usually did not exceed 7–10%. During milling, characteristic chips were collected, as well as worn milling cutters and their fragments, which were then examined using X-ray diffraction (*XRD*) and scanning electron microscopy (*SEM*).

For milling, carbide end mills (*H10F* grade cemented carbide) with a diameter of $\boldsymbol{d}$ = 12 mm were used, manufactured by *PC MION LLC* (Tomsk) (Fig. 3). These tools did not have a wear-resistant coating to reduce the number of factors that could affect the purity of the experiment. The universal geometry of the milling cutters is as follows: flank angle $\boldsymbol{\alpha}$ = +10°, rake angle $\boldsymbol{\gamma}$ = +8°; helix angle $\boldsymbol{\omega}$ = +40°, number of teeth $\boldsymbol{z}$ = 4, cutting edge rounding radius $\boldsymbol{r}$ = 4 ± 2 μm.

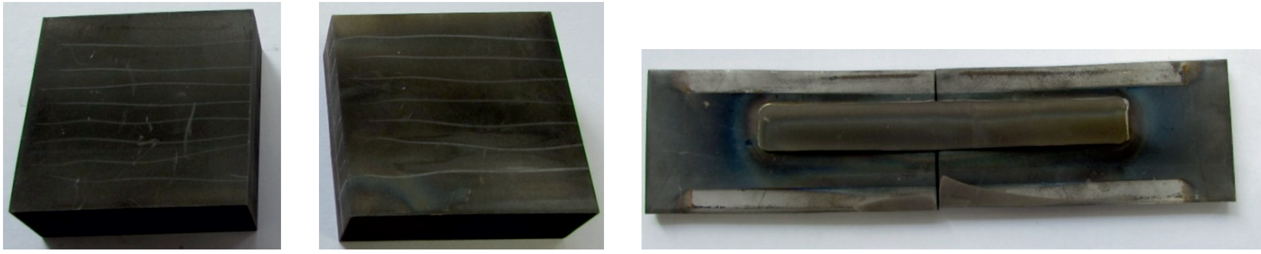

a *b*

Fig. 2. Appearance after electrical discharge machining:
a – samples prepared for milling; *b* – steel backing

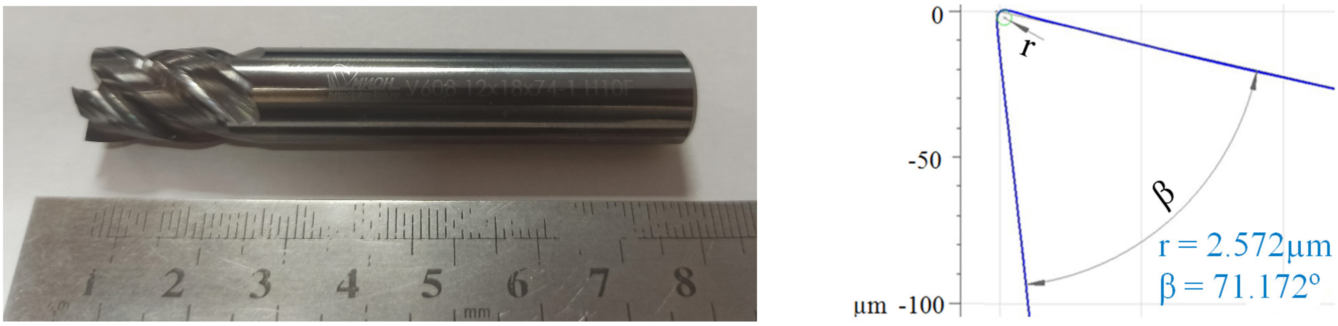

a *b*

Fig. 3. Image of the cutting edge section (*a*) with an indication of the microgeometry measurement fragment (*b*)

The use of a milling cutter with a diameter of 12 mm is due to the fact that the cost of the tool increases in proportion to the square of the diameter. An increase beyond 12 mm entails a significant increase in the cost of tooling when multiple measurements are required to obtain reliable data. Milling cutters with a larger diameter than those used in this experiment make it possible to work with increased feed and milling width; however, the economic feasibility of this approach is assessed as extremely low. On the other hand, increasing the diameter may create limitations when milling thin-walled and small workpieces within the framework of combined additive-subtractive technology (Fig. ***4***).

The following components of the cutting force were measured:

– ***Pf*** is the force directed along the feed direction (feed force);

– ***Pv*** is the force directed perpendicular to the feed direction (lateral force);

– ***Px*** is the force directed along the axis of the milling cutter (axial force).

These forces continuously change due to changes in the uncut chip thickness [22].

When the milling cutter rotates, the orientation of the two basic components of the cutting force changes: tangential ***Pz*** (acts along the direction of the cutting speed, perpendicular to the radius vector from the axis of rotation to the cutting edge) and radial ***Py*** (acts along the radius vector from the cutting edge to the axis of rotation of the milling cutter). These components are primary, but they cannot be measured directly during milling due to the rotation of the tool tooth. Based on ***Pz*** and ***Py***, the ***Pf*** and ***Pv*** forces are formed, which were recorded using a *Kistler* turning dynamometer model *9257BA*.

The ***Ph*** feed force coincides with the direction of the ***Pz*** force at the beginning of the milling cutter tooth cutting into the workpiece, but when the milling cutter rotates and the ***Pz*** force rotates, this component begins to change in favor of increasing the lateral $\boldsymbol{P_v}$ force. On the other hand, at the beginning of the cutting process, the lateral ***Pv*** component is directed together with the radial ***Py*** force. When the milling cutter rotates, the orientation of ***Py*** changes, which causes an increase in the ***Pf*** feed force. In the case of a sharp cutting edge and with a helix angle $\omega = 40°$, the axial ***Px*** force can be oriented away from the workpiece (vertically upwards), which leads to the milling cutter tending to tear off or lift the workpiece. These effects are described in more detail in reference [23].

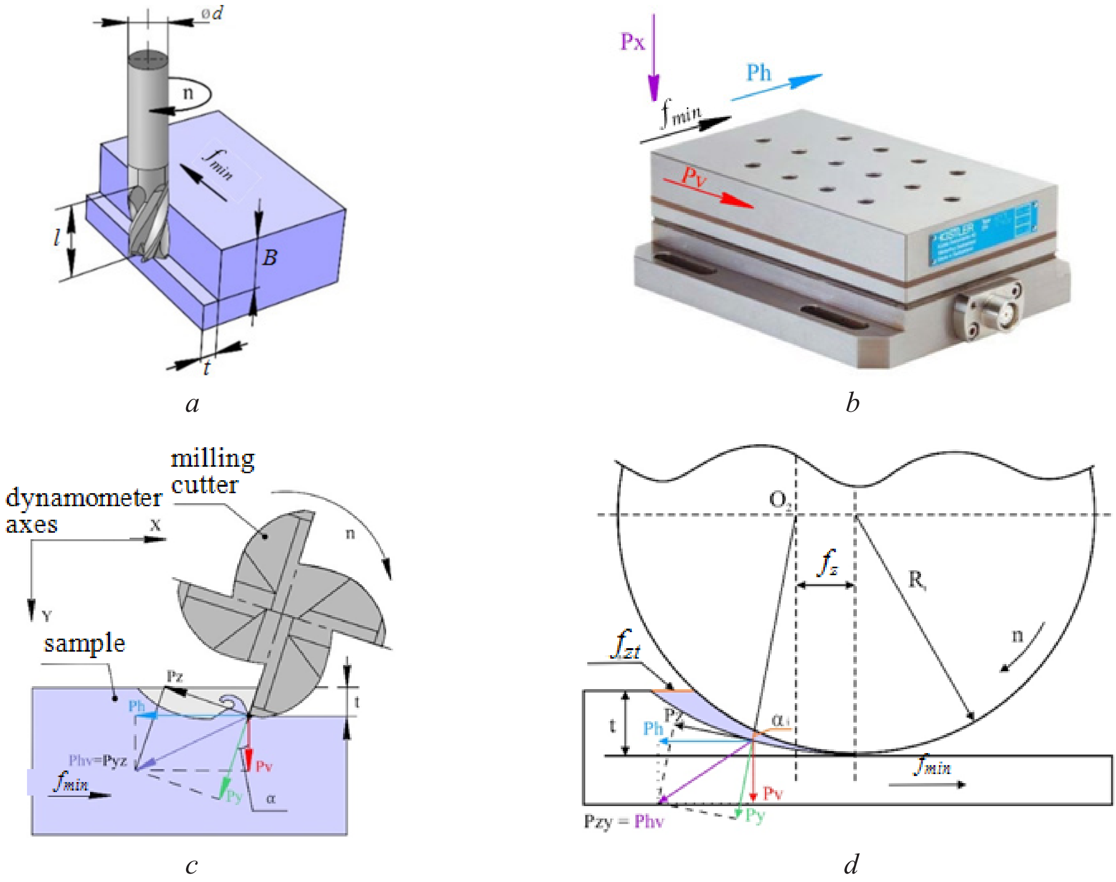

Fig. 4. Milling parameters (*a*) and schematic diagrams of cutting force components acting on the milling cutter relative to the dynamometer coordinate system (*b*, *c*, *d*)

In the course of preliminary experiments, it was revealed that with climb milling, compared with conventional milling under the same modes ($\boldsymbol{n}$ = 315 rpm, $\boldsymbol{B}$ = 7 mm, $\boldsymbol{t}$ = 1 mm, $\boldsymbol{S}_{min}$ = 25 mm/min), the values of the maximum component forces $\boldsymbol{Ph}_{max}$ and $\boldsymbol{Pv}_{max}$ are 3–6 times higher. The same results were found for other cutting modes up to a feed of 250 mm/min, but with a feed of more than 80 mm/min, noticeable vibrations begin, which sometimes leads to overload and malfunction of the *DynoWare* program, as well as to chipping of the cutting edge of the milling cutter, which makes it difficult to repeat the machining repeatedly to determine the confidence interval.

This phenomenon is explained by the kinematics of climb milling. When cutting into the workpiece, the uncut chip thickness is at its greatest. In addition, the direction of the tangential force ***Pz***, as the largest cutting force, is directed toward the workpiece, and with a small milling depth $\boldsymbol{t}$ = 1 mm, it approximately coincides with the direction of the lateral force ***Pv***. The thicker chips formed during cutting into the workpiece press on the workpiece from the rake surface, and with a small chip contact length with the rake surface (due to the small arc length of the cutting edge contact with the workpiece because of the small milling depth $\boldsymbol{t}$), the chip retains its pressure even before the cutting edge leaves contact with the workpiece, when the uncut chip thickness tends to zero. This process is aggravated by the high viscosity of the *Inconel 625* alloy, and its low thermal conductivity leads to an increase in temperature in the cutting area, which causes chips to adhere to the rake surface of the milling teeth. A similar effect of the kinematics of climb milling is observed in the machining of other materials [23, 24, 27]; as a result, its use is justified only for finishing – with a small feed rate and a high rotation speed of the milling cutter, i.e., when the maximum uncut chip thickness is small. In this case, there is an advantage over conventional milling, in which the machined material is pressed under the cutting edge at the initial moment of tooth entry. Considering this circumstance, all the main experiments were carried out with conventional milling.

The milling modes adopted in this work, indicated in Table 1, were obtained experimentally during preliminary work. The limitation in the choice of modes was premature breakage of the teeth or the milling cutters themselves during operation within the first 10 seconds.

Table 1

Milling parameters of *Inconel 625*

Test No.	Milling cutter rotation speed $\boldsymbol{n}$, (rpm)	Cutting speed $\boldsymbol{v}$, (m/min)	Feed rate $\boldsymbol{S}_{min}$, (mm/min)	Depth of cut $\boldsymbol{t}$ ($\boldsymbol{a}_e$), mm	Width of cut $\boldsymbol{B}$ ($\boldsymbol{a}_p$), mm
1	315	11.9	25	1	7
2			50		
3			80		
4			200		
5	630	23.8	25		
6			50		
7			80		
8			200		

To be able to increase the feed rate to 250 mm/min, the milling width was assumed to be 7 mm [23].

The experimental data recorded during the measurements were subjected to statistical processing based on classical methods of mathematical statistics and the theory of experimental planning. In particular, we calculated a sample mean with a 95% confidence interval using *Student's* ***t***-distribution, estimated the extreme values, and also used the *bootstrap* method. The calculation procedures were automated using the *STATISTICA v.8* application package.

Phase analysis of the blanks and milling cutters was performed on an X-ray diffractometer model *DRON-8H* (NPP *"Burevestnik"*, St. Petersburg) using *CuKα* radiation with a step of 0.05° and an exposure time of 20 s per step. Microstructural images, images of chips, and wear zones were obtained on two scanning electron microscopes (*SEM*): a *MIRA 3 LMU* (*Tescan*, Czech Republic), equipped with a module for energy-dispersive microanalysis (*EDX*) with a nitrogen-free detector model *Ultim MAX 40*; and a high-resolution *SEM* with field emission model *Apreo 2 S* (*ThermoFisher* Scientific, USA), equipped with an energy-dispersive X-ray spectroscopy (*EDS*) detector model *Octane Elect*.

The microstructure, chemical composition, and properties of the initial sample were studied using standardized techniques using a metallographic microscope model *Axio Observa 1m* (*Carl Zeiss*, Germany); a portable X-ray fluorescence analyzer model *S1 TITAN SPX* (*Bruker*, USA); a stationary microhardness tester model *DuraScan-10*; and a universal testing machine model *50ST* (*Tinius* Olsen, USA). The microgeometry of the milling edges (sharpness, roughness) was measured using a high-precision non-contact method on an *EdgeMaster* installation (*Alicona*, Austria).

Results and discussion

The results of the chemical analysis are shown in Table 2.

The *Inconel 625* sample under consideration is based on the mechanism of dispersion hardening [21]. After etching, a uniform dendritic distribution is recorded in the structure, where the grain boundaries

Table 2

Chemical composition of the wire and the test sample

Test object and the requirements of the standard	Mass fraction of elements (%)										
	C	*Si*	*Mn*	*Cr*	*Mo*	*Ni*	*Al*	*Cu*	*Ti*	*Fe*	*Nb+Ta*
Inconel 625 sample	<0.1	0.3	0.3	21.5	9.0	63.5	0.4	–	0.4	0.5	3.7
GOST 5632-2014		<0.5	<0.5	20…23	8…10	>58	<0.4	–	<0.4	<5.0	3.2…4.2

are clearly identified. The analysis of the transition areas, as well as the fusion zones of the wire layers, reveals the presence of columnar morphology. The origin of the latter is due to the fact that the previously crystallized metal was subjected to secondary heating (Fig. 5, *a*).

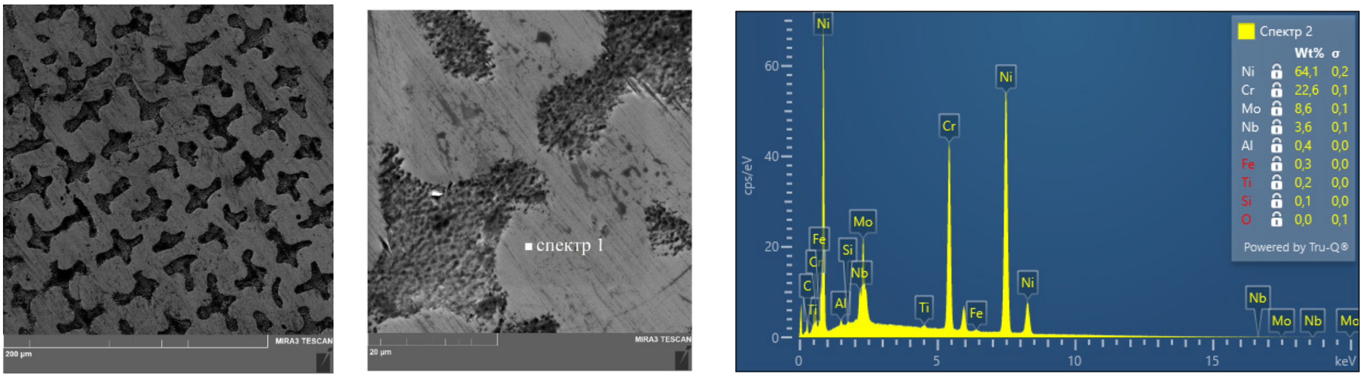

a *b* *c*

Fig. 5. Microstructure fragment of the *Inconel 625* sample in the longitudinal section (***ZOX***):
a, *b* – magnifications ×1,240 and ×6,220, respectively; *c* – intensity distribution map at point "Spectrum 1"

In Figs. 5,*a* and *b*, the dark areas correspond to the boundaries of **γ**-Ni dendrites that appeared after chemical etching. The formation of dendritic morphology is associated with incomplete mutual solubility of phases based on *Ni* and *Cr*. This process is accompanied by the formation of fine particles of alloyed carbides (*Mo*, *Nb*, *Ti*), as shown in Fig. 5,*b*. These inclusions are localized mainly in areas enriched in *Ni* (in the image they appear as light gray areas).

Fig. 6 shows the phase composition of the *Inconel 625 EBAM* alloy sample. Diffraction reflections at angles of 43.5°, 50.5°, 74.5° and 90.5° are recorded on the X-ray diffractogram for the state before milling. These peaks are identified as reflections from crystallographic planes (111), (200), (220) and (311), belonging to a solid solution of **γ**-*Ni*. Therefore, **γ**-*Ni* is the base phase of the sample.

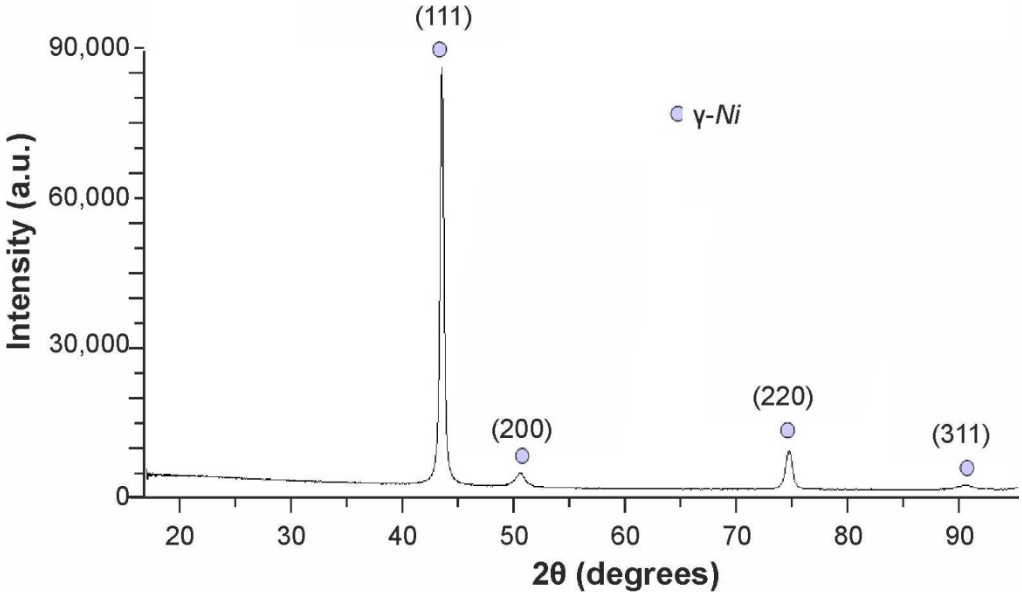

Fig. 6. X-ray diffraction pattern of the *Inconel 625* sample

According to the data obtained, the hardness of the *Inconel 625* samples under study varies from 200 to 246 HV. Table 3 shows the evaluated mechanical characteristics of the material.

The phase composition of the cutting edges of the new milling cutter is represented by two phases: *WC* and *Co* (see Fig. 7).

Table 3

Mechanical properties of *Inconel 625* as a function of the build direction

Section	*UTS* (σ_u) (MPa)	σ_y (MPa)	δ_5, %
ZOY (transverse)	640 ± 20	144 ± 14	56 ± 3
ZOX (longitudinal)	647 ± 80	171 ± 5	61 ± 3

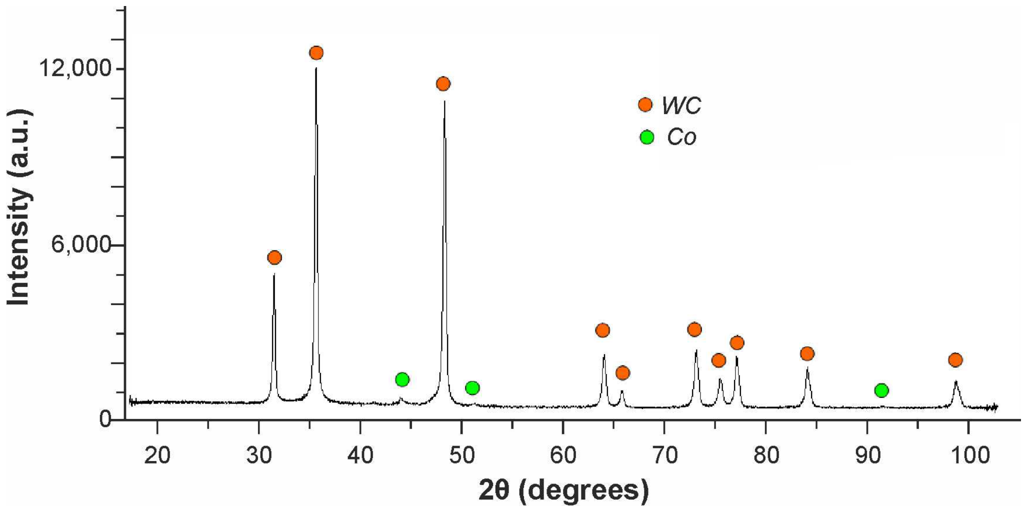

Fig. 7. X-ray diffraction pattern of the cutting edge surface of the milling cutter before milling

Based on measurements of the forces over time using a dynamometer, the maximum values of the cutting force components were obtained (see Fig. 8). All measurements were repeated 4–5 times not only within one day but also over several days to determine the confidence interval, which showed that the difference in readings for the same mode does not exceed 7–10%. When constructing the graphs, the results obtained on the same day that showed the greatest forces were used for the subsequent guaranteed calculation of the milling cutter strength.

Fig. 9 shows graphs of the effect of the S_{min} feed rate on the largest magnitude of the component cutting forces in the direction of milling *Inconel 625* longitudinally and transversely the feed direction during sample synthesis.

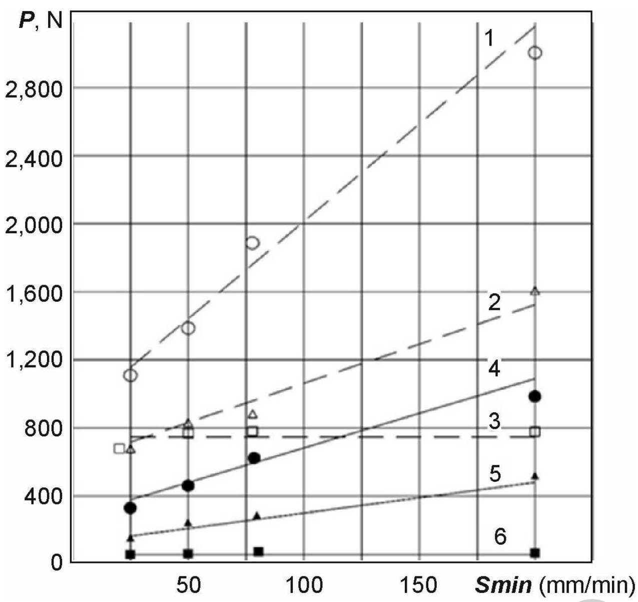

Fig. 8. Effect of the feed rate S_{min} and cutting speed v on the maximum cutting force components during up-milling of *Inconel 625* with a 12 mm diameter milling cutter:

v = 11.9 m/min: 1 – (○) Ph_{max}; 2 – (Δ) Pv_{max}; 3 – (□) Px_{max}
v = 23.8 m/min: 4 – (●) Ph_{max}; 5 – (▲) Pv_{max}; 6 – (■) Px_{max}

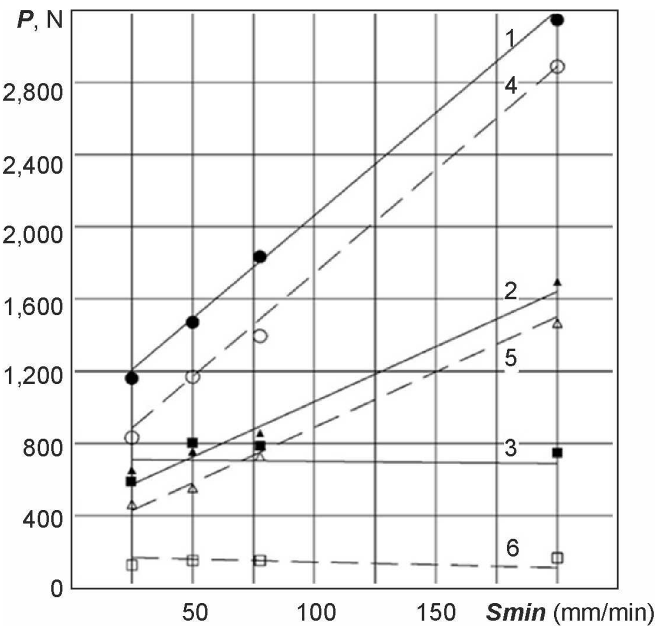

Fig. 9. Effect of the feed rate $\boldsymbol{S}_{\mathbf{min}}$ on the maximum cutting force components during up-milling at a constant cutting speed $\boldsymbol{v}$ = 11.9 m/min:
along the feed direction during synthesis: 1 – (●) $\boldsymbol{Ph}_{\mathbf{max}}$; 2 – (▲) $\boldsymbol{Pv}_{\mathbf{max}}$; 3 – (■) $\boldsymbol{Px}_{\mathbf{max}}$;
across the feed direction during synthesis: 4 – (○) $\boldsymbol{Ph}_{\mathbf{max}}$; 5 – (∆) $\boldsymbol{Pv}_{\mathbf{max}}$; 6 – (□) $\boldsymbol{Px}_{\mathbf{max}}$

In a series of experiments, the milling width ***B*** was assumed to be 7 mm, and the cutting depth ***t*** was 1 mm. This choice of modes is due to the desire to achieve maximum productivity while maintaining the operability of the end mill and ensuring acceptable economic costs.

Previous experimental studies [24] have shown that with a constant cross-sectional area of the cut (product ***B***×***t***), it is preferable to increase the milling width. When trying to increase the cutting depth, it was noted that the chips stay longer in the chip groove, and their volume increases and, under the influence of high temperatures, adhesion intensifies, leading to compaction.

Increasing the feed rate increases the volume of metal remaining in the groove throughout the entire contact period during cutting. A lump of compacted chips is formed, which, warming up due to friction, acquires a bright red glow and becomes even more firmly welded to the groove. This phenomenon occurs only in one of the chip grooves, and attempts to remove the formed lump lead to damage to the cutting edge. Practical experience has shown that milling with a depth ***t*** of no more than 1 mm is an effective way to ensure chip removal.

The data shown in Fig. 9 indicate that the maximum value of the feed force $\boldsymbol{Ph}_{max}$ increases more intensively compared to the lateral force $\boldsymbol{Pv}_{max}$. At the same time, the dependences of both values in both the longitudinal and transverse directions demonstrate an almost identical character. When milling along the synthesis direction, the $\boldsymbol{Ph}_{\mathbf{max}}$ and $\boldsymbol{Pv}_{\mathbf{max}}$ forces slightly exceed the similar values obtained when milling transversely. In our view, this difference is explained by the higher yield strength of the material in the longitudinal direction relative to the transverse direction (see Table 3).

The amplitude of the axial force $\boldsymbol{Px}_{\mathbf{max}}$ remains unchanged as the feed increases. However, when milling longitudinally, it turns out to be significantly larger than when milling transversely. Cross-milling is characterized by a cyclical change in the sign of the $\boldsymbol{Px}_{\mathbf{max}}$ force (from minus to plus). This phenomenon causes vibration instability during cutting. For example, when milling small workpieces that are fixed only from the sides, a negative value of the ***Px*** force can lead to the workpiece being pulled out of the fixture – the clamping force is insufficient. This problem also occurs when machining thin-walled workpieces or those with insufficient rigidity, where the use of high clamping forces is impossible.

Based on experimental data (see Figs. 8 and 9), linear dependences of cutting forces on feed were determined at cutting speeds $\boldsymbol{v}$ = 11.9 m/min and 23.8 m/min (Table 4).

Milling modes that ensure maximum productivity (see Table 2) are characterized by accelerated increased wear of the cutting edges and chip sticking to the flank surface, as well as compaction of the chip in the chip groove (see Fig. 10), and very high values of cutting forces (see Figs. 8–9).

When trying to use a feed of more than 250 mm/min, the milling edges inevitably failed in the first seconds of milling due to breakage (Fig. 11). In this regard, the feed was limited to 200 mm/min.

Table 4

Regression equations describing the effect of the feed rate S_{min} on the maximum cutting force components

v = 11.9 m/min; S_{min} = 25–200 mm/min			v = 23.8 m/min; S_{min} = 25–200 mm/min		
Ph_{max}	Pv_{max}	Px_{max}	Ph_{max}	Pv_{max}	Px_{max}
$9.8 \cdot S_{min} + 854$ $R^2 = 0.87$	$4.8 \cdot S_{min} + 508$ $R^2 = 0.89$	$0.2 \cdot S_{min} + 675$ $R^2 = 0.85$	$4.9 \cdot S_{min} + 237$ $R^2 = 0.88$	$2.4 \cdot S_{min} + 100$ $R^2 = 0.91$	$-0.11 \cdot S_{min} + 132$ $R^2 = 0.93$

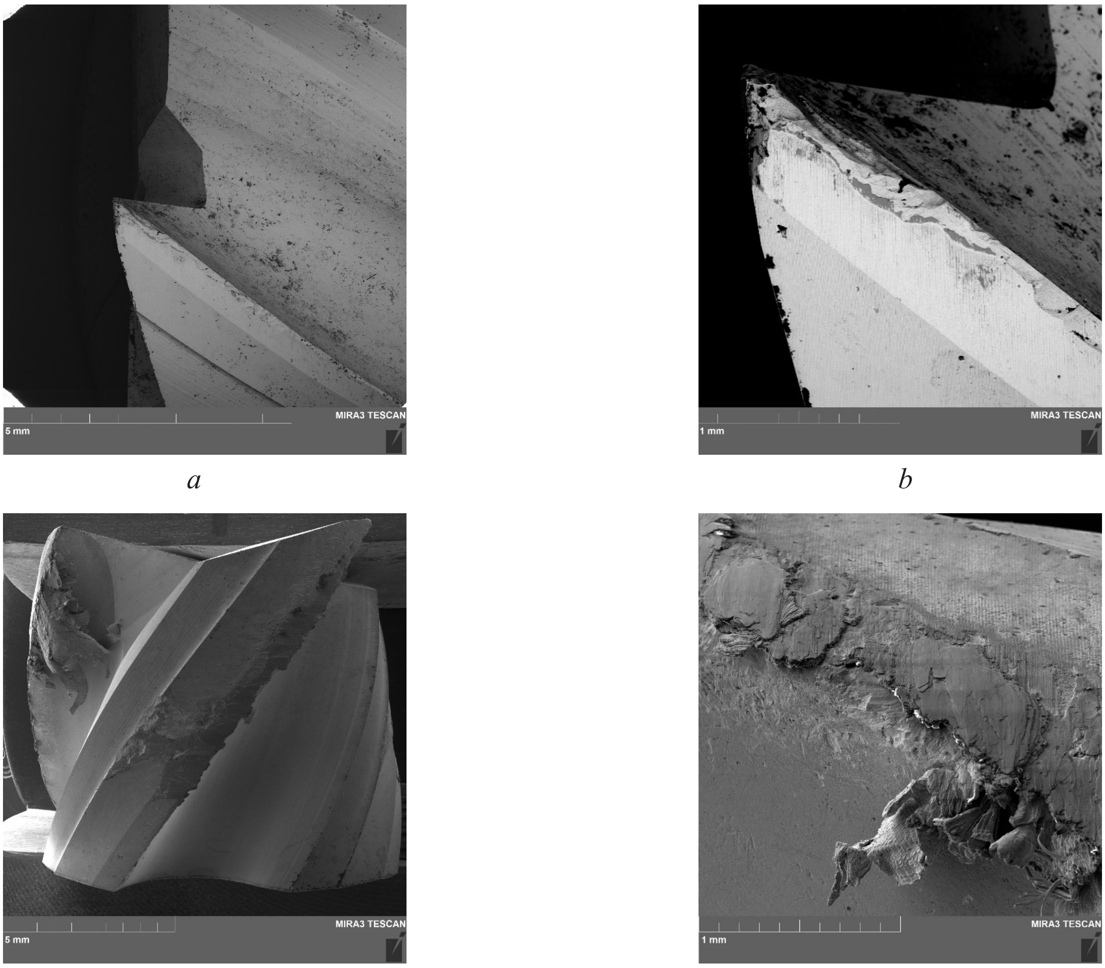

a *b* *c* *d*

Fig. 10. SEM images of the cutting edges of cemented carbide end mills:
a, *b* – after approximately 5 minutes of operation (magnification ×59 and ×207); *c*, *d* – after critical wear (magnification ×35 and ×155)

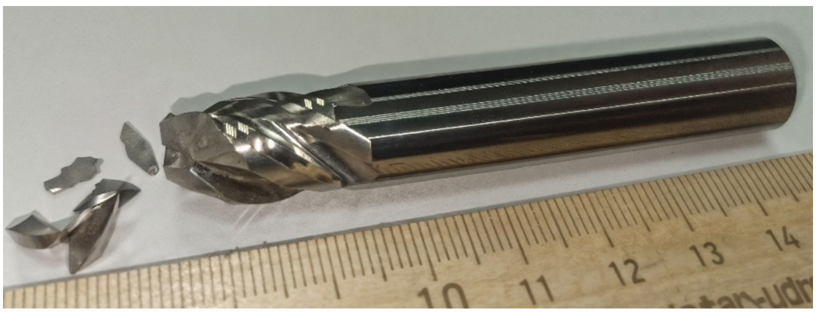

Fig. 11. Photograph of a typical fracture of the cutter teeth

The X-ray structure analysis of the cutting edges performed after milling showed that in addition to the initial *WC* and *Co* phases, they contain phases formed as a result of thermomechanical interaction between the elements of the milling cutter material and the workpiece being processed. The adhering fragments contain complex $Cr_{23}C_6$ carbide and *NiW* intermetallic compound (see Figs. 12, *a*, *b*). *SEM* data indicate the presence of a large accumulation of firmly welded chips that overhang the rake surface (see Fig. 12, *c*).

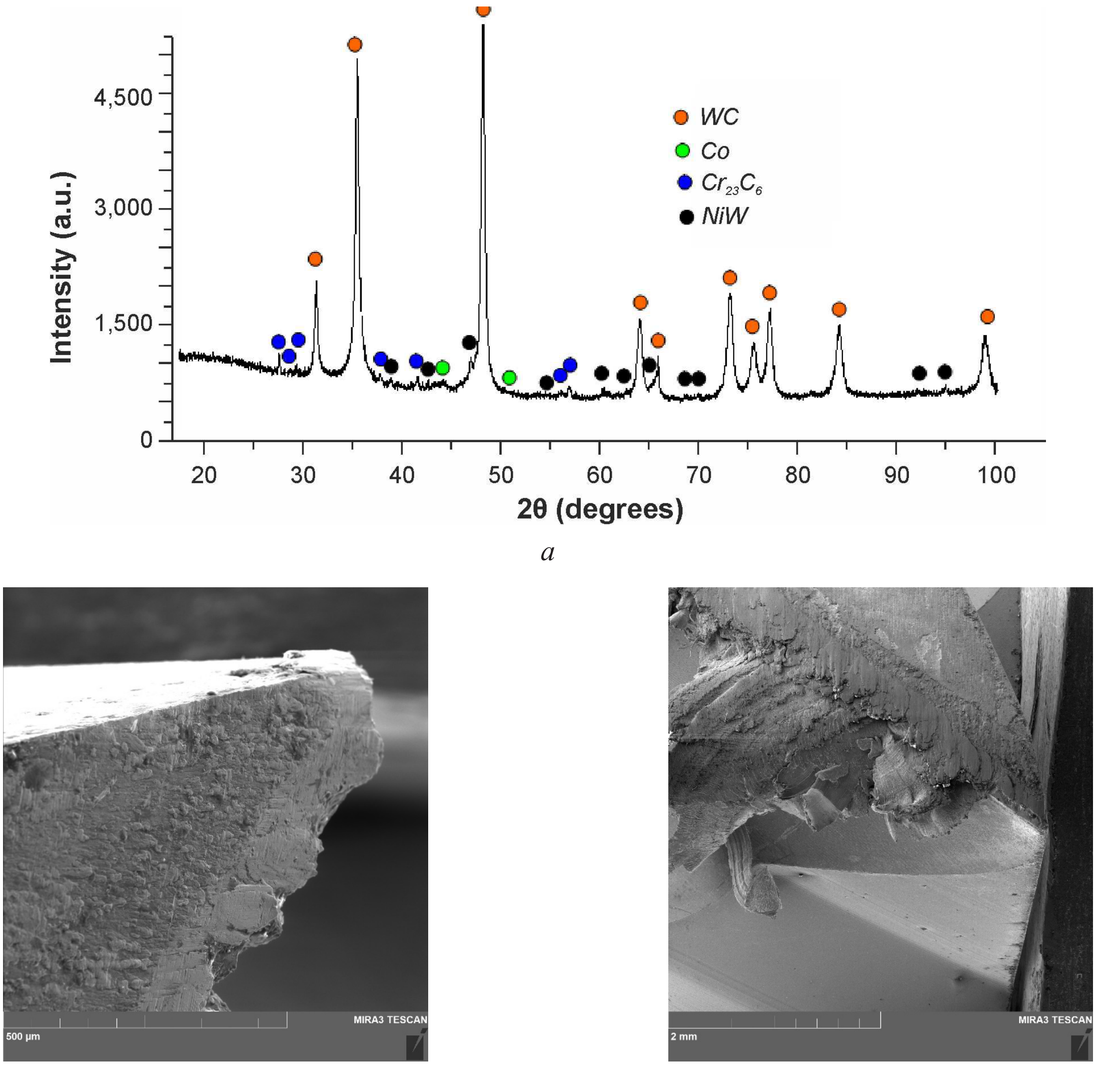

a

b *c*

Fig. 12. X-ray diffraction pattern (*a*) and SEM micrographs (*b*, *c*) of the cutting edges of the milling cutter after milling (magnification ×414 and ×78, respectively)

No oxygen-containing phases were detected during the analysis of the cutting edges. Consequently, the oxidative component of the wear mechanism of the tool material under the conditions of the experiments is insignificant.

Adhesive processes during cutting ensure the interaction between the elements of the workpiece and the structural elements of the tool. Under the influence of coupling forces, one or a group of grains of tool material is displaced. The result is a significant weakening of the cutting edge, which manifests itself in the form of chipping or breakage.

Let us take a closer look at the micrographs and morphology of the characteristic chips (Fig. 13) obtained by milling using the modes from Table 1.

In the photos (see Fig. 13), a part of the chip is shown, and its width is measured in the vertical direction (see Fig. 14, *c*). On the cutting edge along the helical surface of the milling cutter, the chip width ***b*** is ≈ 4.5 mm. However, it is less than the contact length along the main cutting edge, which is 10.9 mm (see Figs. 14, *a*, *b*).

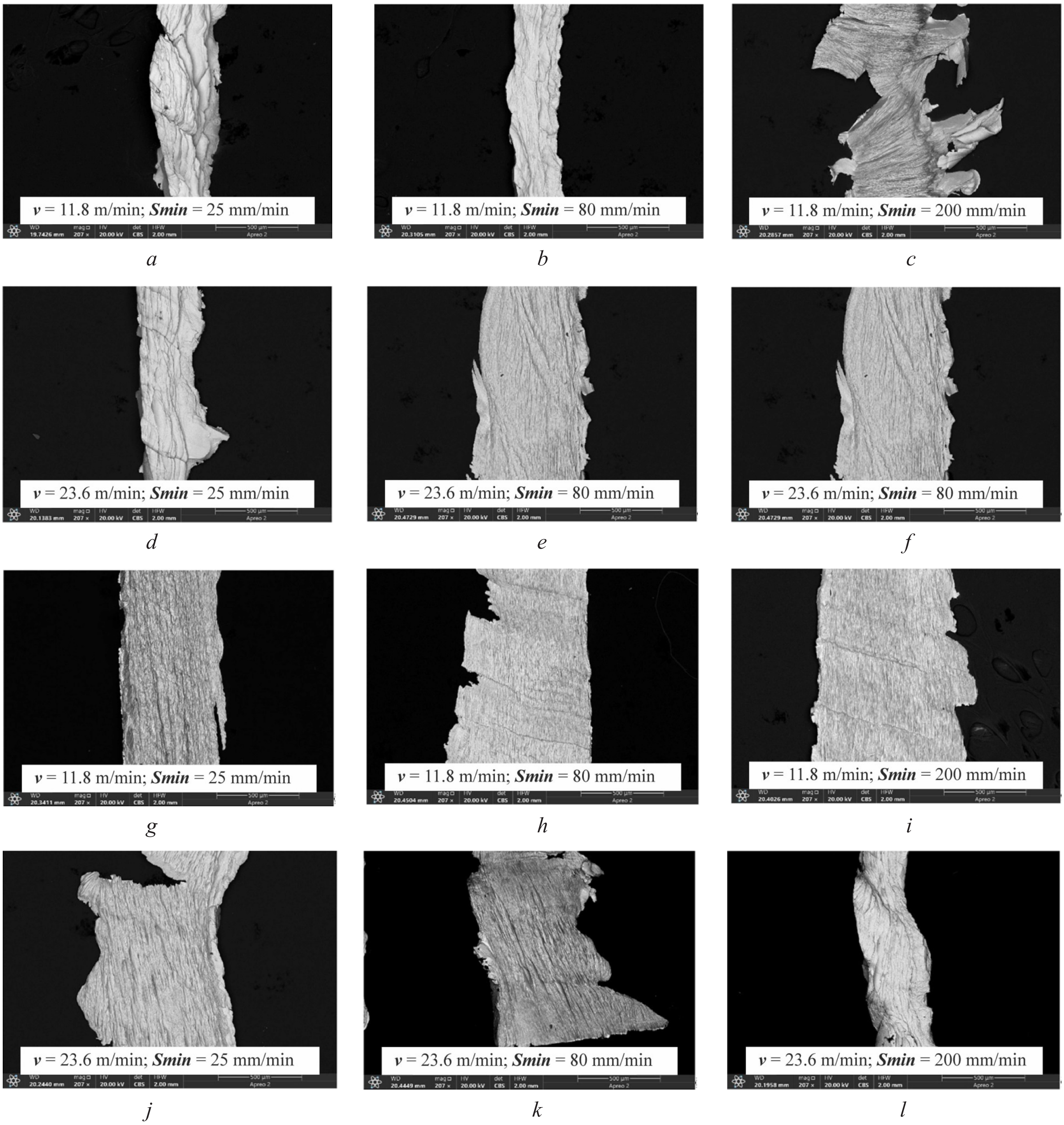

Fig. 13. Micrographs of chips obtained under various milling conditions (magnification ×207):
a–f – along the build direction; *g–l* – across the build direction

A small milling depth $\boldsymbol{t}$ = 1 mm (radial depth $\boldsymbol{a_e}$ in English terminology) leads to a decrease in the maximum contact length of the main cutting edge with the vertical machined surface $\boldsymbol{l_{contact\_t}}$. The latter, in turn, depends on the length of the arc of contact between the tip of the milling cutter tooth and the surface of the workpiece $\boldsymbol{l_{arc}}$ for a given milling diameter $\boldsymbol{d}$, milling depth $\boldsymbol{t}$, and feed per tooth $\boldsymbol{S_z}$ (mm/tooth), i.e., $\boldsymbol{l_{arc}} = \boldsymbol{f}(\boldsymbol{d}, \boldsymbol{t}, \boldsymbol{S_z})$. Since the diameter of the milling cutter and the depth of milling did not change during the experiments, the arc length $\boldsymbol{l_{arc}}$ depends only on the feed per tooth.

The feed per tooth is calculated using the well-known formula $\boldsymbol{S_z} = \boldsymbol{S_{min}} / (\boldsymbol{n} \times \boldsymbol{z})$, where $\boldsymbol{S_{min}}$ is the feed rate (mm/min); $\boldsymbol{n}$ is the rotational speed of the milling cutter (rpm); $\boldsymbol{z}$ is the number of teeth. Thus, with the lowest feed used, $\boldsymbol{S_{min}}$ = 25 mm/min and the lowest used milling cutter speed, $\boldsymbol{n}$ = 315 rpm, S_z = 0.02 mm/tooth, then

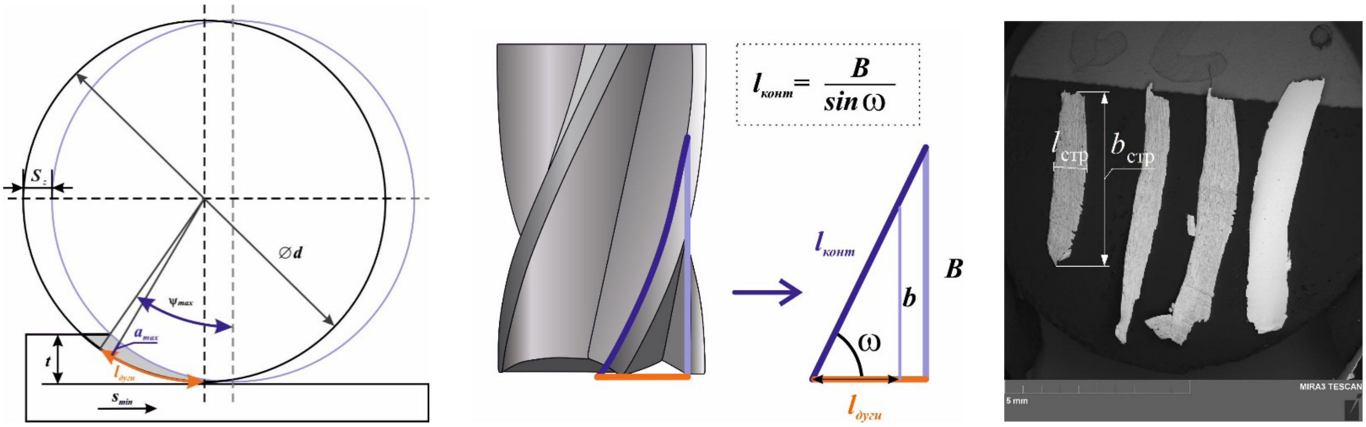

a *b* *c*

Fig. 14. Diagrams for determining:

a – the length of the contact arc between the tooth tip and the workpiece; *b* – the contact length between the cutting edge and the vertical workpiece surface when the cutter tooth is fully engaged; *c* – the main chip parameters

$\boldsymbol{l}_{arc}$ = 3.2 mm. At the highest feed rate, $\boldsymbol{S}_{min}$ = 200 mm/min and $\boldsymbol{n}$ = 315 rpm, $\boldsymbol{S}_z$ = 0.159 mm/tooth, $\boldsymbol{l}_{arc}$ = 3.42 mm. Thus, despite an 8-fold increase in feed per tooth, the arc length increased by only 1.07 times. Thus, the main influence on the length of the arc of contact between the tip of the tooth and the sample is exerted by the milling cutter diameter ***d*** and the milling depth ***t***. In the diagram in Fig. 14, the amount of feed per tooth $\boldsymbol{S}_z$ is shown schematically 6 times more than it actually is, even with the highest feed per tooth $\boldsymbol{S}_{z\_max}$ = 0.159 mm/tooth ($\boldsymbol{S}_{min}$ = 200 mm/min and $\boldsymbol{n}$ = 315 rpm).

It is noted that the longest contact length of the main cutting edge with the vertical machined surface is $\boldsymbol{l}_{contact\_t}$ = 1 mm = $\boldsymbol{l}_{arc}$ / cos **ω** = 3.42 / cos 40° = 4.46 mm, which corresponds to the chip width ($\boldsymbol{b}_{chip}$ ≈ 4.5 mm).

Perpendicular to the helical main cutting edge, the chips move along the rake surface of the milling cutter tooth. The chip length $\mathbf{l}_{chip}$ in this direction (in the photo, Fig. 13, this corresponds approximately to the horizontal size of the chip without considering its twisting) with a feed rate of $\boldsymbol{S}_{min}$ = 25 mm/min and $\boldsymbol{n}$ = 315 rpm is $\boldsymbol{l}_{chip}$ ≈ 0.3 mm (see Fig. 13, *a*).

An increase in the feed rate to 200 mm/min at $\boldsymbol{n}$ = 315 rpm leads to an increase in the chip length to $\boldsymbol{l}_{chip}$ ≈ 1 mm (see Fig. 13, *c*), and its width increases to $\boldsymbol{b}_{chip}$ ≈ 10 mm. An increase in the chip width from 4.5 to 10 mm is associated, in our opinion, with an increase in temperature as a result of an increase in feed, and the welding of the next chip section in width, i.e., these sections move like a continuous ribbon because the next section pushes the previous one along the helical chip groove upward even after passing the top of the cutting edge of its arc length $\boldsymbol{l}_{arc}$ (see Figs. 14, *a*, *b*). This is due to the fact that the sections of the cutting edge located above the top continue to cut the chips and push them up along the helical groove until the entire main cutting edge comes out of contact with the vertical surface of the sample with a height of ***B***, or milling width of ***B*** = 7 mm. Therefore, with an increased feed rate, $\boldsymbol{b}_{chip}$ ≈ $\boldsymbol{l}_{contact\_full}$ = 10.9 mm. The chips are not divided into parts by width, but some chips have dull cracks that precede the separation of the chips into parts by width (see Fig. 13, *d*).

Here and further, it is mentioned that the temperature in the cutting zone (in the zone of primary plastic deformations) increases with increasing feed, cutting speed, and other parameters of the cutting mode, although the cutting temperature was not directly measured due to technical complexity. Based on the results of experimental studies by the authors [3, 4, 16, 27] and considering the phenomena observed in this work, a correlation has been established with the generally accepted provisions on the effect of uncut chip thickness and cutting speed on cutting temperature.

As the rotational speed increases to 630 rpm ($\boldsymbol{v}$ = 23.8 m/min) at $\boldsymbol{S}_{min}$ = 25 mm/min, the feed per tooth decreases to $\boldsymbol{S}_z$ = 0.01 mm/tooth, but the chip length increases to 0.55 mm (see Fig. 13, *d*). This is 1.8 times more than with a lower cutting speed of $\boldsymbol{v}$ = 11.9 m/min and the same feed per tooth. The reason for this phenomenon is twofold: first, an increase in temperature in the area of primary plastic deformation, and second, an increase in the plasticity of the machined material under heating conditions. In addition, if at a cutting speed of $\boldsymbol{v}$ = 11.9 m/min the chips were rolled up into a tube (see Fig. 13,*a*), which made it difficult to measure their true length, then at $\boldsymbol{v}$ = 23.8 m/min the chips are flatter (see Fig. 13,*d*).

An increase in the feed rate to 200 mm/min at $\boldsymbol{v}$ = 23.8 m/min (feed per tooth $\boldsymbol{S}_z$ = 0.08 mm/tooth) leads to an increase in chip length to 1.55 mm (see Fig. 13, *f*). In width, the chips begin to split into approximately equal parts with a width of 0.6 mm, loosely fixed to each other. On the one hand, such an effect can cause a decrease in forces on the rake surface of the tooth, but, on the other hand, an increase in chip length and a decrease in its twisting lead to a deterioration in chip placement in the chip groove, and with a further increase in cutting or feed speed, it causes its negative packing.

When milling transversely to the feed direction during synthesis, the chips differ from longitudinal milling in the absence of torsion even at the lowest feed rates (see Fig. 13). In contrast to the twisted shape of the chips during longitudinal milling at feed rates of 25 and 80 mm/min at $\boldsymbol{n}$ = 315 rpm (see Figs. 13, *a*, *b*), the chips are formed flat (see Figs. 13, *g*, *h*), which, as mentioned above, makes them difficult to remove. At the highest feed rate of 200 mm/min, the chips are long and wide but with a ragged shape (see Fig. 13, *c*), whereas with transverse feed they are solid (see Fig. 13,*i*). Nevertheless, the magnitude of the ***Pf*** and ***Pv*** forces in transverse milling is slightly less than in longitudinal milling at all feeds, and the axial force ***Px*** is almost 4 times less (see Fig. 9).

An increase in the cutting speed to 23.8 m/min did not change the shape of the chips when milling transversely to the synthesis direction (see Figs. 13, *j*, *k*), and at 80 m/min, the shape of the chips during transverse and longitudinal milling is approximately the same. However, when the feed is increased to 200 mm/min, the chips become, on the contrary, twisted (see Fig. 13,*l*), as opposed to straight chips during longitudinal milling (see Fig. 13, *f*).

The outer side of the chips has small folds parallel to the chip width (see Fig. 15), which are the vertices of elements of the pseudo-continuous chip, which is typical when machining not-very-ductile materials or when machining metals that work harden under large plastic deformation. Thus, in the zone of primary plastic deformation, the formed element shifts along the shear surface, but high temperature and pressure lead to welding of these chip elements. With an increase in feed, there is a more significant separation of the chip elements due to an increase in the uncut chip thickness [34], but the tops of the elements can only be seen at high magnification.

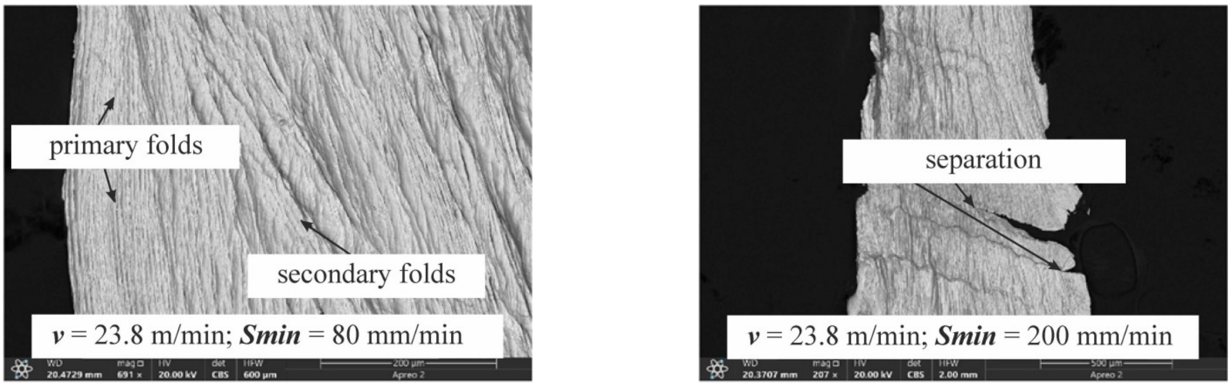

a *b*

Fig. 15. Typical *SEM* micrographs of chips:

a – formation of folded structures; *b* – formation and propagation of a main crack

Micrographs of the chips obtained using *SEM* show areas with embedded *WC* grains on the rake surface (see Fig. 16). It has been established that an increase in milling loads leads to the appearance of larger fragments of tool material on the rake surface of the chip – up to 150 μm or more in size. This observation is an indirect sign of adhesive fatigue wear. Its essence is that high-temperature exposure combined with

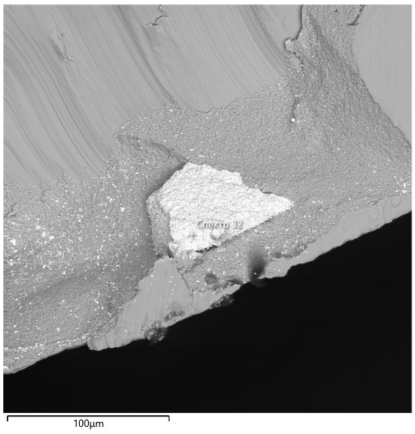

a

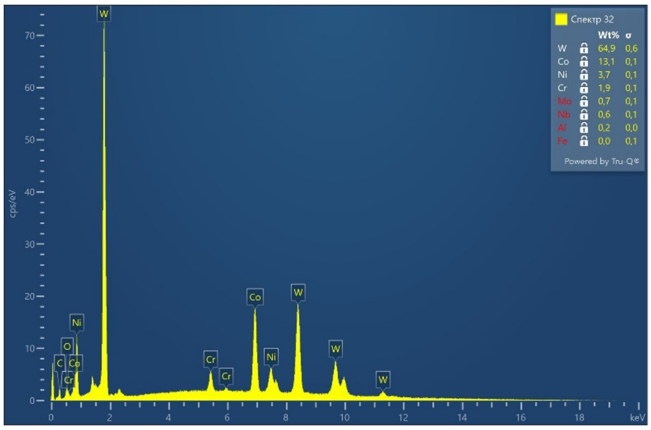

b

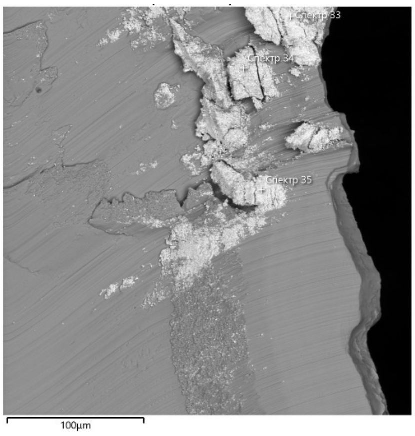

c

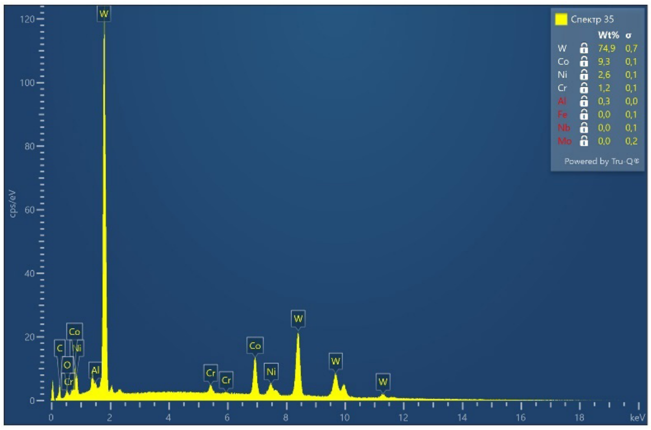

d

Fig. 16. SEM micrographs and *EDX* analysis of the rake surface of chips:
a, *b* – conditions: 23.8 m/min, 80 mm/min; *c*, *d* – conditions: 23.8 m/min, 200 mm/min

accumulated stresses in the surface layer of the tool weakens the cobalt bond. As a result, *WC* grains break off and are transferred to the rake surface of the chip.

The study of possible structural and phase transformations occurring in the machined material under high-temperature exposure and deformation was performed by X-ray diffraction. The chips [26] formed at different cutting speeds and feed rates, as well as the surface of the sample after milling, were analyzed (Fig. 17).

On the surface of the workpiece after milling and in the chips obtained at $\boldsymbol{v}$ = 11.9 m/min, $\boldsymbol{S}_{min}$ = 25 mm/min and 200 mm/min (see Fig. 17), the formation of new phases compared to the initial state of the material before milling was not detected (see Fig. 6). At the same time, it was noted that the X-ray texture, which was observed in the initial state and is caused by dendritic growth characteristic of additive materials [27], noticeably weakens after milling, both on the machined surface and in the chips (see Fig. 16). This texture is manifested in the predominant orientation of the (111) **γ**-*Ni* planes.

To quantify the degree of texture before and after milling *Inconel 625*, the texture coefficient was calculated. The latter were calculated for the initial *Inconel 625* sample before milling, for the *Inconel 625* sample after milling, and for the chips, and these data were compared with texture coefficients calculated from peak intensities taken from the standard database for **γ**-*Ni* (00-023-0297) (Fig. 18).

These results confirm two facts. First, the initial *Inconel 625* has a pronounced texture before milling, due to dendritic growth. Second, after milling, a weakening of this texture is recorded on the surface of the workpiece, as well as in the chips. This decrease in texture intensity is presumably due to the effects of significant plastic deformations. Under their influence, the initial highly textured structure undergoes changes that cause spontaneous disorientation of the crystallographic planes of the machined material.

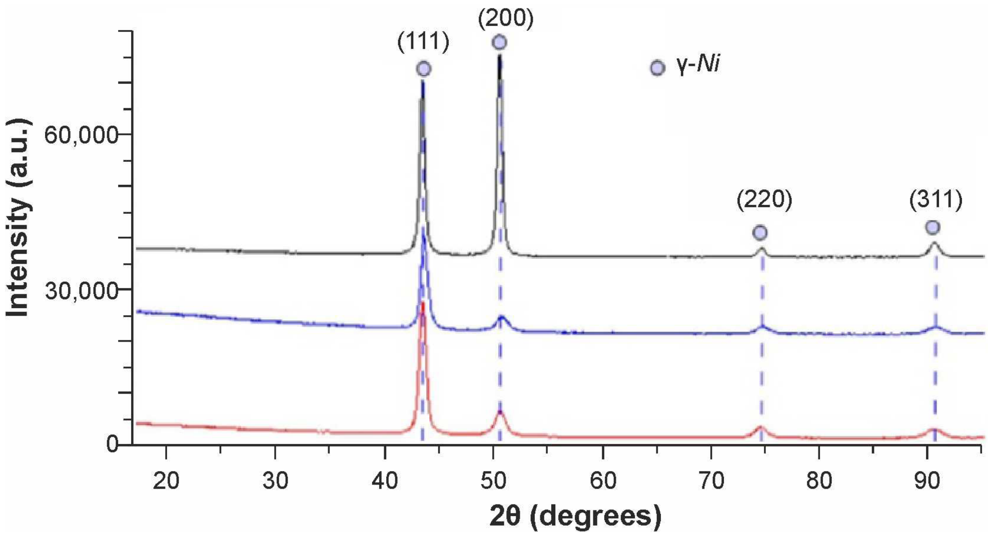

Fig. 17. X-ray diffraction patterns (milling along the build direction):
1 – *Inconel 625* after milling (***v*** = 23.8 m/min, S_{min} = 200 mm/min); 2 – chips (***v*** = 11.9 m/min, S_{min} = 200 mm/min); 3 – chips (v = 11.9 m/min, S_{min} = 5 mm/min)

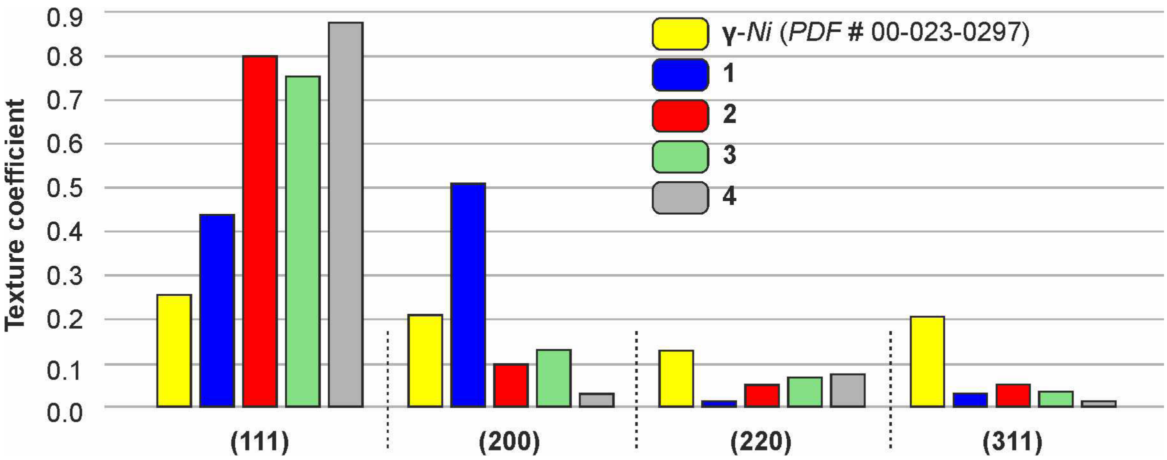

Fig. 18. Texture coefficients calculated from the X-ray diffraction patterns shown in Figs. 7 and 19 compared with those obtained from the standard database:
1 – *Inconel 625* after milling (***v*** = 23.8 m/min, S_{min} = 200 mm/min); 2 – chips (***v*** = 11.9 m/min, S_{min} = 200 mm/min); 3 – chips (***v*** = 11.9 m/min, 2 S_{min} = 5 mm/min); 4 – initial *Inconel 625* sample before milling

In addition to reducing the severity of the X-ray texture on the surface after milling and in the chips, structural changes were identified within the framework of this study. They are expressed in the broadening of diffraction reflections compared to the initial level, which is a typical sign of the occurrence of intense plastic deformations (see Fig. 19).

Furthermore, the peaks in the samples and chips shifted relative to the initial state to the region of larger angles after milling (see Fig. 19), which is a sign of a decrease in the lattice parameter of cubic γ-*Ni* in the chips and may be associated with an increased level of compressive stresses.

It is customary to describe the wear of an uncoated carbide tool during cutting using three mechanisms: abrasive, adhesive, and oxidative [28]. At low speeds, abrasive wear dominates due to the low temperature, which is insufficient to activate other mechanisms.

In the case of machining nickel-based superalloys, abrasive wear is characteristic [30] due to the presence of particles of solid carbides and oxides in the machined material, which form characteristic

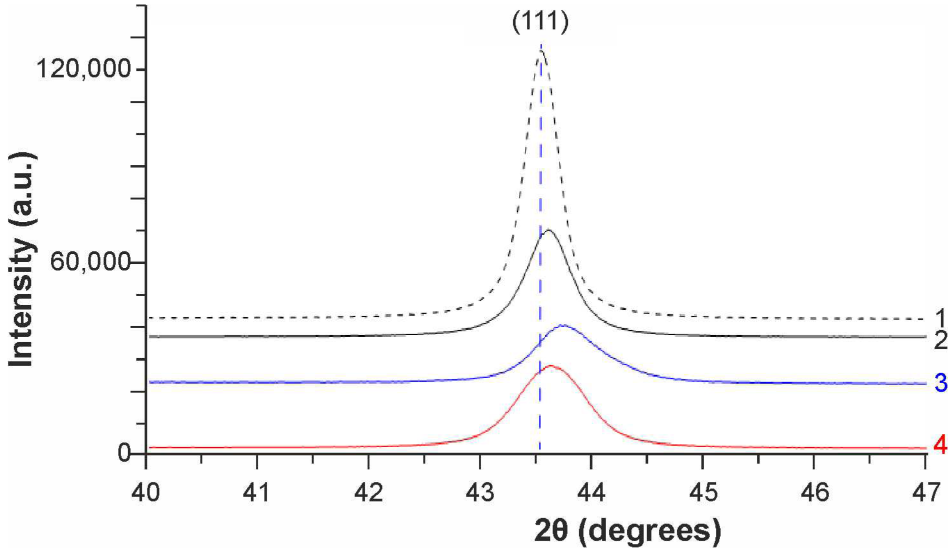

Fig. 19. X-ray diffraction patterns:

1 – initial *Inconel 625* sample; 2 – *Inconel 625* after milling ($\boldsymbol{v}$ = 23.8 m/min, $\boldsymbol{S}_{\mathbf{min}}$ = 200 mm/min); 3 – chips ($\boldsymbol{v}$ = 11.9 m/min, $\boldsymbol{S}_{\mathbf{min}}$ = 200 mm/min); 4 – chips ($\boldsymbol{v}$ = 11.9 m/min, $\boldsymbol{S}_{\mathbf{min}}$ = 25 mm/min)

grooves (scratches) on the rake and flank surfaces. At the same time, with increasing temperature, the role of oxidative wear may increase, which accelerates the abrasive processes of tool wear.

Adhesive wear occurs at high pressures and temperatures on the rake surface of the tool at the point of its contact with the chips. Under the influence of these factors, intense plastic deformation is activated, leading to the exposure of fresh surface layers. The adsorption of atoms of interacting materials occurs with the formation of interatomic bonds, forming bonding sites. The relative movement of the milling cutter tooth and the workpiece causes the destruction of these bonds, which leads to displacement or pull-out of individual grains or groups of them. Thus, wear due to adhesion is realized.

Plastic deformation of the tool material is associated with creep at high temperatures [31]. The cobalt bond is deformed more intensively, since its creep resistance at high temperatures is insufficient [32]. The softening of the cobalt bond causes WC grains to pull out of the structure of the tool material.

The presence of adhesive interaction between the machined material and the tool during the cutting process is evidenced by two circumstances. First, the elements *W*, *Co*, *Ni*, and *Cr* were found on the rake surface of the chips (see Fig. 16). Second, after milling, the formation of new phases $Cr_{23}C_6$ and *NiW* was recorded on the cutting edges of the *WC-Co* milling cutter (see Fig. 12). It is suggested that under the action of the coupling forces arising between the elements of the machined material and the tool material, the displacement of one or more adjacent tool grains is initiated. The result is a significant weakening of the cutting edge, which can cause its destruction. Based on the above, to minimize adhesive wear, cutting modes should be assigned on a scientific basis.

The conditions for the occurrence of oxidative wear are tight contact of the rake surface of the tool with the chips and simultaneous contact of the flank surface with the machined surface of the workpiece. At the point of such contact, friction develops with high intensity, which is accompanied by the active release of thermal energy. The low thermal conductivity inherent in *Inconel 625* alloy leads to extremely high temperatures in the tool-chip interface. Under these conditions, *Co* and *WC* interact with oxygen from the air to form oxides (*CoO*, WO_3, Co_3O_4, etc.), which impair the cutting properties of the tool and cause increased wear [33].

Within the framework of this study, the signs of oxidative wear were not confirmed. The *EDX* method did not detect oxygen (see Fig. 16), and X-ray diffraction did not detect oxygen-containing phases on the cutting edges of the milling cutter after milling (see Fig. 12). Thus, the contribution of oxidative wear to the destruction of the cutting tool in this work can be considered insignificant.

Conclusions

1. As a result of the conducted research, it was found that milling of *Inconel 625* alloy obtained using *EBAM* additive technology is accompanied by very high cutting forces. As the feed rate increases, the ***Pf*** force increases more intensively than the lateral ***Pv*** force. Anisotropy of machinability was found: when milling along the direction of synthesis, the cutting forces slightly exceed the corresponding values when milling transversely, which corresponds to a higher yield strength in the longitudinal direction.

2. For cutting speeds of 11.9 and 23.8 m/min, linear regression models were obtained describing the dependence of the cutting force components on the feed rate. An increase in the cutting speed in the specified range is accompanied by a decrease in the absolute values of cutting forces, but at the same time the chip length increases, which complicates its evacuation along the chip groove from the cutting area. It was found that *Inconel 625 EBAM* in the as-built state is characterized by a reduced yield strength (144–171 MPa) due to its coarse-grained columnar structure and lack of dispersion hardening, but retains a pronounced anisotropy of properties (≈ 19% difference between longitudinal and transverse directions), which must be taken into account when assigning cutting modes.

3. It is shown that chip morphology significantly depends on the cutting modes. With increasing feed and cutting speed, there is an increase in chip length (up to 1.55 mm or more), the disappearance of its twisting, and the appearance of deep cracks, which, with further intensification of the modes, leads to chip compaction in the chip groove and tool breakage. In cross-milling, even at low feed rates, in contrast to the twisted shape of the chips in longitudinal milling, the chips form flat chips, which makes chip removal difficult. However, this does not increase the milling forces.

4. It has been established that the dominant mechanism of wear of carbide end mills during machining of *Inconel 625* obtained using *EBAM* additive technology is adhesive fatigue wear. This is evidenced by the detection of *WC* particles of tool material on the rake surfaces of the chips, as well as the presence of $Cr_{23}C_6$ and *NiW* phases on the cutting edges, formed as a result of the thermomechanical interaction of the tool material and the workpiece.

5. X-ray diffraction analysis showed that the milling process leads to a decrease in the initial crystallographic texture of the additively obtained material, a broadening of diffraction peaks, and their displacement, which indicates the occurrence of intense plastic deformation in the surface layer of the workpiece and the chips. Despite machining without coolant, no oxygen-containing phases were found on the cutting edges, which indicates an insignificant role of oxidative wear under the studied milling conditions.

6. Rational milling modes have been experimentally determined (conventional feed, cutting speed no more than 23.8 m/min, feed rate up to 200 mm/min, cutting depth 1 mm, milling width 7 mm), ensuring the operability of the carbide tool. Exceeding a feed rate of 250 mm/min leads to catastrophic chipping of the cutting edges within the first seconds of cutting.

References

1. M'Saoubi R., Outeiro J.C., Chandrasekaran H., Dillon O.W. Jr., Jawahir I.S. A review of surface integrity in machining and its impact on functional performance and life of machined products. *International Journal of Sustainable Manufacturing*, 2008, vol. 1 (1–2). pp. 203–236. DOI: 10.1504/IJSM.2008.019234.

2. Yue C., Gao H., Liu X., Liang S.Y. Part functionality alterations induced by changes of surface integrity in metal milling process. *Applied Sciences*, 2018, vol. 8. DOI: 10.3390/app8122550.

3. Kaya E., Akyüz B. Effects of cutting parameters on machinability characteristics of Ni-based superalloys. *Open Engineering*, 2017, vol. 7, pp. 330–342. DOI: 10.1515/eng-2017-0037.

4. Deshpande Y.V., Andhare A.B., Padole P.M. How cryogenic techniques help in machining of nickel alloys? *Machining Science and Technology*, 2018, vol. 22, pp. 543–584 DOI: 10.1080/10910344.2017.1382512.

5. Cai X., Qin S., Li J., An Q., Chen M. Experimental investigation on surface integrity of end milling nickel based alloy – Inconel 718. *Machining Science and Technology*, 2014, vol. 18. DOI: 10.1080/10910344.2014.863627.

6. Devillez A., Le Coz G., Dominiak S., Dudzinski D. Dry machining of Inconel 718, workpiece surface integrity. *Journal of Materials Processing Technology*, 2011, vol. 211. DOI: 10.1016/j.jmatprotec.2011.04.011.

7. Deshpande Y.V., Binani S., Singh A., Mohatkar M., Chatpalliwar A.S., Barve P.S. Enhancing the machinability of Inconel 625 milling using cryogen and blend of biodegradable oils and application of advanced algorithms. *Journal of the Brazilian Society of Mechanical Sciences and Engineering*, 2023, vol. 45, art. 587. DOI: 10.1007/s40430-023-04509-y.

8. Silva R.H.L., Schoop J., Hassui A., Jawahir I.S. Inconel 625 sustainable milling surface integrity and the dependence on alloy processing route. *The International Journal of Advanced Manufacturing Technology*, 2024, vol. 130, pp. 4493–4512. DOI: 10.1007/s00170-023-12938-1.

9. Akgün M., Demir H. Optimization and finite element modelling of tool wear in milling of Inconel 625 superalloy. *Journal of Polytechnic*, 2021, vol. 24 (2), pp. 391–400. DOI: doi.org/10.2339/politeknik.706605.

10. Akgün M., Demir H. Estimation of surface roughness and flank wear in milling of Inconel 625 superalloy. *Surface Review and Letters*, 2021, vol. 28 (4). DOI: 10.1142/S0218625X21500116.

11. Jarosz K., Patel K.V., Özel T. Mechanistic force modeling in finish face milling of additively manufactured Inconel 625 nickel-based alloy. *The International Journal of Advanced Manufacturing Technology*, 2020, vol. 111, pp. 1535–1551. DOI: 10.1007/s00170-020-06222-9.

12. Abeni A., Loda D., Özel T., Attanasio A. Analytical force modelling for micro milling additively fabricated Inconel 625. *Production Engineering*, 2020, vol. 14, pp. 613–627. DOI: 10.1007/s11740-020-00980-x.

13. Rodrigues M.A., Hassui A., Silva R.H.L., Loureiro D. Tool life and wear mechanisms during Alloy 625 face milling. *The International Journal of Advanced Manufacturing Technology*, 2016, vol. 85, pp. 1439–1448. DOI: 10.1007/s00170-015-8056-4.

14. Tascioglu E., Kaynak Y., Poyraz Ö., Orhangül A., Ören S. The effect of finish-milling operation on surface quality and wear resistance of Inconel 625 produced by selective laser melting additive manufacturing. *Advanced Surface Enhancement*, Singapore: Springer, 2020, pp. 263–272. DOI: 10.1007/978-981-15-0054-1_27.

15. Chauhan S., Trehan R., Singh R.P. Classification of surface roughness for CNC face milling of Inconel 625 superalloy utilizing cutting force signal features with SVM and ANN. *Materials Today: Proceedings*, 2023, vol. 113, pp. 9–18. DOI: 10.1016/j.matpr.2023.07.101.

16. Raval P., Patel D., Prajapati R., Badheka V., Gupta M.K., Khanna N. Energy consumption and economic modelling of performance measures in machining of wire arc additively manufactured Inconel-625. *Sustainable Materials and Technologies*, 2022, vol. 32. DOI: 10.1016/j.susmat.2022.e00434.

17. Fei J., Liu G., Patel K., Özel T. Effects of machining parameters on finishing additively manufactured nickel-based alloy Inconel 625. *Journal of Manufacturing Materials Processing*, 2020, vol. 4. DOI: 10.3390/jmmp4020032.

18. Kaynak Y., Tascioglu E. Finish machining-induced surface roughness, microhardness and XRD analysis of selective laser melted Inconel 718 alloy. *Procedia CIRP*, 2018, vol. 71, pp. 500–504. DOI: 10.1016/j.procir.2018.05.013.

19. Alonso U., Veiga F., Suárez A., Del Val A.G. Characterization of Inconel 718® superalloy fabricated by wire arc additive manufacturing: effect on mechanical properties and machinability. *Journal of Materials Research and Technology*, 2021, vol. 14, pp. 2665–2676. DOI: 10.1016/j.jmrt.2021.07.132.

20. Kalashnikov K., Kalashnikova T., Semenchuk V., Knyazhev E., Panfilov A., Cheremnov A., Chumaevskii A., Nikonov S., Vorontsov A., Rubtsov V., Kolubaev E. Development of a multimaterial structure based on CuAl9MN2 bronze and Inconel 625 alloy by double-wire-feed additive manufacturing. *Metals*, 2022, vol. 12 (12). DOI: 10.3390/met12122048.

21. Boltrushevich A.E., Martyushev N.V., Kozlov V.N., Kuznetsova Yu.S. Struktura zagotovok iz splava Inconel 625, poluchennykh elektrodugovoi naplavkoi i naplavkoi s pomoshch'yu elektronnogo lucha [Structure of Inconel 625 alloy blanks obtained by electric arc surfacing and electron beam surfacing]. *Obrabotka metallov (tekhnologiya, oborudovanie, instrumenty) = Metal Working and Material Science*, 2024, vol. 26, no. 4, pp. 206–217. DOI: 10.17212/1994-6309-2024-26.4-206-217.

22. Choi J.G., Yang M.Y. In-process prediction of cutting depths in end milling. *International Journal of Machine Tools and Manufacture*, 1999, vol. 39 (5), pp. 705–721. DOI: 10.1016/S0890-6955(98)00067-4.

23. Babaev A.S., Kozlov V.N., Semenov A.R., Shevchuk A.S., Ovcharenko V.A., Sudarev E.A. Issledovanie sil rezaniya i obrabatyvaemosti pri frezerovanii poroshkovoi korrozionno-stoikoi stali, poluchennoi po tekhnologii pryamogo lazernogo vyrashchivaniya (LMD) [Investigation of cutting forces and machinability during milling of corrosion-resistant powder steel produced by laser metal deposition]. *Obrabotka metallov (tekhnologiya, oborudovanie, instrumenty) = Metal Working and Material Science*, 2024, vol. 26, no. 2, pp. 38–56. DOI: 10.17212/1994-6309-2024-26.2-38-56.

24. Arlyapov A., Volkov S., Promakhov V., Matveev A., Babaev A., Vorozhtsov A., Zhukov A. Study of the machinability of an Inconel 625 composite with added NiTi-TiB2 fabricated by direct laser deposition. *Metals*, 2022, vol. 12. DOI: 10.3390/met12111956.

25. Rahman M.A., Rahman M., Woon K.S., Mia M. Episodes of chip formation in micro-to-nanoscale cutting of Inconel 625. *International Journal of Mechanical Sciences*, 2021, vol. 199. DOI: 10.1016/j.ijmecsci.2021.106407.

26. Li G., Xu W., Jin X., Liu L., Ding S., Li C. The machinability of stainless steel 316 L fabricated by selective laser melting: Typical cutting responses, white layer and evolution of chip morphology. *Journal of Materials Processing Technology*, 2023, vol. 315. DOI: 10.1016/j.jmatprotec.2023.117926.

27. Kocaman E., Gürol U., Günen A., Çam G. Effect of post-deposition heat treatments on high-temperature wear and corrosion behavior of Inconel 625. *Materials Today Communications*, 2025, vol. 42. DOI: 10.1016/j.mtcomm.2024.111101.

28. Liu E., An W., Xu Z., Zhang H. Experimental study of cutting-parameter and tool life reliability optimization in Inconel 625 machining based on wear map approach. *Journal of Manufacturing Processes*, 2020, vol. 53, pp. 34–42. DOI: 10.1016/j.jmapro.2020.02.006.

29. Yıldırım Ç.V., Sarıkaya M., Kıvak T., Şirin Ş. The effect of addition of hBN nanoparticles to nanofluid-MQL on tool wear patterns, tool life, roughness and temperature in turning of Ni-based Inconel 625. *Tribology International*, 2019, vol. 134, pp. 443–456. DOI: 10.1016/j.triboint.2019.02.027.

30. Akhtar W., Sun J., Sun P., Chen W., Saleem Z. Tool wear mechanisms in the machining of Nickel based super-alloys: a review. *Frontiers of Mechanical Engineering*, 2014, vol. 9, pp. 106–119. DOI: 10.1007/s11465-014-0301-2.

31. Astakhov V.P. The assessment of cutting tool wear. *International Journal of Machine Tools and Manufacture*, 2004, vol. 44, pp. 637–647. DOI: 10.1016/j.ijmachtools.2003.11.006.

32. Ayed Y., Germain G., Ammar A., Furet B. Degradation modes and tool wear mechanisms in finish and rough machining of Ti17 Titanium alloy under high-pressure water jet assistance. *Wear*, 2013, vol. 305 (1–2), pp. 228–237. DOI: 10.1016/j.wear.2013.06.018.

33. Liu E., Wang N., Qi J., Xu Z., Liu X., Zhang H. Experimental study on the oxidation and diffusion behavior of Inconel 625 and tool materials. *Crystals*, 2018, vol. 8 (12). DOI: 10.3390/cryst8120471.

34. Kozlov V., Babaev A., Schulz N., Semenov A., Shevchuk A. Study of a methodology for calculating contact stresses during blade processing of structural steel. *Metals*, 2023, vol. 13 (12). DOI: 10.3390/met13122009.

Conflicts of Interest

The authors declare no conflict of interest.